Joint ISRF and Spectral Shift Estimation for Spectrometer Calibration using Optimal Transport

Jihanne El Haouari
TéSA, ENSEEIHT/IRIT/Univ. Toulouse
Toulouse, France
jihanne.elhaouari@tesa.prd.fr

Filip Elvander
Aalto University
Espoo, Finland
filip.elvander@aalto.fi

Jean-Yves Tourneret
ENSEEIHT/IRIT/Univ. Toulouse, TéSA
Toulouse, France
jean-yves.tourneret@toulouse-inp.fr

Herwig Wendt
CNRS, Univ. Toulouse
Toulouse, France
herwig.wendt@irit.fr

Jean-Michel Gaucel
Thales Alenia Space Cannes
Cannes, France
jean-michel.gaucel@thalesaleniaspace.com

Christelle Pittet
Centre National d'Etudes Spatiales
Centre Spatial de Toulouse, France
christelle.pittet@cnes.fr

***Abstract*—The estimation of high-resolution spectrometer instrument spectral response functions (ISRFs) is crucial, for example in the context of remote sensing in order not to compromise the determination of trace gas concentrations. This paper introduces a new statistical model and an optimization algorithm for the joint estimation of ISRFs and spectral shifts. As a key novel ingredient, we investigate the use of optimal transport theory and the associated Wasserstein distance to estimate the spectral shifts, comparing this approach to the conventional ℓ_2 norm. As a second key ingredient, a sparse representation of the ISRFs is used to decompose these functions into a fixed dictionary of atoms. Results suggest that the proposed method performs well for small spectral shifts with both distances, while the Wasserstein distance proves particularly effective for estimating larger spectral shifts.**

***Index Terms*—Instrument spectral response function (ISRF), Spectral shifts, Optimal transport, Wasserstein distance, Sparsity.**

I. Introduction

Context and related work. High-resolution spectrometers, such as the CNES/UKSA MicroCarb instrument, play a vital role in remote sensing applications, including monitoring gas fluxes and retrieving atmospheric trace gas concentrations. For the MicroCarb mission, currently under study by the Centre National d'Etudes Spatiales (CNES) in Toulouse, France [1], achieving the expected accuracy in determining CO_2 concentrations requires precise knowledge of the instrument spectral response functions (ISRFs) at the relevant wavelengths. Each pixel on the spectrometer detector is associated with a unique ISRF, which can vary across the entire wavelength range. The wavelength corresponding to each pixel is defined as the center of the ISRF at that pixel. Spectral calibration requires precise characterization of both the shape of the ISRFs and the specific wavelengths at which they are centered. The measured spectrum, denoted as $s(\lambda_l)$, at a given wavelength λ_l associated with a given pixel l is the result of a convolution between the ISRF for that pixel, denoted as I_l, and a high-resolution reference spectrum r [2], [3]:

$$s(\lambda_l) = \sum_{n=-N/2}^{N/2} r(\lambda_l - n\Delta) I_l(n\Delta) + \epsilon_l, \qquad (1)$$

where Δ is the spacing between the $N+1$ points of the ISRF wavelength grid, λ_l is the measured wavelength (which is not necessarily on the same grid as the ISRF), and ϵ_l is Gaussian noise associated with the lth measurement. Initial ISRF wavelength characterization is typically performed on the ground. However, spectral shifts can arise due to factors such as imperfect calibration, Doppler shifts, red light effects, or thermoelastic errors [4], [5]. These shifts cause the ISRF to be centered at a displaced wavelength, $\lambda_l' = \lambda_l + \delta(l)$, leading to errors in the peak locations of the spectrum, as illustrated in Fig. 1, but also to a slight modification of the values of the measured spectrum. A realignment is needed to minimize the discrepancy between the measured and true spectra. Note that the spectral shifts $\delta(l)$ generally depend on the wavelength.

Recent studies have explored the use of sparse representations for ISRF estimation, being more effective than traditional parametric models like Gaussian or generalized Gaussian functions [6]. However, no prior work has addressed the joint estimation of both ISRFs and unknown spectral shifts.

Goals, Contributions, and Outline. The objective of this work is to introduce a new approach for estimating jointly the ISRFs and spectral shifts during spectrometer calibration. The first contribution is the definition of a statistical model that enables the joint estimation of ISRFs and spectral shifts (see Section II), along with the proposed optimization algorithm. The second contribution is the use of a new metric based on optimal transport (OT) theory for estimating spectral shifts (see Section III). Experiments are conducted on data simulated by CNES for the MicroCarb mission, covering two levels of spectral shifts. The results are presented in Section IV and demonstrate the effectiveness of the proposed approach in jointly estimating spectral shifts and ISRFs. Finally, conclusions and future works are reported in Section V.

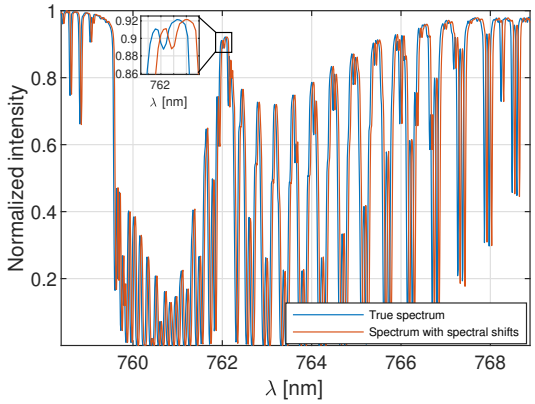

Fig. 1. Effect of spectral shifts on the measured spectrum.

II. Joint estimation of ISRFs and spectral shifts

A. Sparse representation of ISRFs

Each specific pixel l of the spectrometer detector has an associated ISRF I_l with the central wavelength λ_l. Only a single measurement (1) is available for each wavelength λ_l, leading to a non-identifiable problem since the ISRFs for different pixels are not identical. However, within a small observation window $\mathcal{W}(\lambda_l) = \left\{\lambda_{l-\frac{L}{2}}, ..., \lambda_{l+\frac{L}{2}}\right\}$ around each wavelength of interest λ_l, the ISRFs do not change significantly, and thus these measurements can be used for ISRF estimation [6]. In vectorial form, (1) can be rewritten as:

$$\boldsymbol{s}_l = \boldsymbol{R}_l \boldsymbol{I}_l + \boldsymbol{\epsilon}_l, l = 1, ..., N_\lambda, \tag{2}$$

where $\boldsymbol{\epsilon}_l \in \mathbb{R}^{L+1}$ is an additive white Gaussian noise and

$$\begin{aligned}
\boldsymbol{s}_l &\triangleq [s(\lambda_{l-\frac{L}{2}}), ..., s(\lambda_{l+\frac{L}{2}})] \in \mathbb{R}^{L+1}, \\
\boldsymbol{R}_l &\triangleq [r(\lambda_{l'} - n\Delta)]_{l-\frac{L}{2} \leq l' \leq l+\frac{L}{2}, \; -\frac{N}{2} \leq n \leq \frac{N}{2}} \in \mathbb{R}^{(L+1)\times(N+1)}, \\
\boldsymbol{I}_l &\triangleq [I_l(-N\Delta/2), ..., I_l(N\Delta/2)] \in \mathbb{R}^{N+1}.
\end{aligned}$$

The matrix $\boldsymbol{R}_l$ therefore contains the reference spectrum $\boldsymbol{r}$ interpolated onto the ISRF wavelength grid for each wavelength within the observation window $\mathcal{W}(\lambda_l)$, i.e.,

$$\boldsymbol{R}_l = \pi(\boldsymbol{r}, \mathcal{W}(\lambda_l)), \quad l = 1, ..., N_\lambda, \tag{3}$$

where $\boldsymbol{r} \in \mathbb{R}^{N_r}$ is the vectorized reference spectrum and the interpolation function $\pi : \mathbb{S} \times \mathbb{W} \to \mathbb{R}^{(L+1)\times(N+1)}$ returns a matrix of $L+1$ shifted versions of the input spectrum (each centered at the wavelengths in the observation window and interpolated at the ISRF wavelengths) and $\mathbb{S}, \mathbb{W}$ are the sets of reference spectra and observation windows $\mathcal{W}(\lambda_l), \quad l = 1, ..., N_\lambda$. Based on previous studies [6], the ISRF $\boldsymbol{I}_l$ of pixel l can be decomposed as follows:

$$\boldsymbol{I}_l \approx \boldsymbol{I}_l^K = \boldsymbol{\Phi}\boldsymbol{\alpha}_l, \tag{4}$$

where $\boldsymbol{\Phi} \in \mathbb{R}^{(N+1)\times N_\mathrm{D}}$ is a dictionary composed of N_D atoms and $\boldsymbol{\alpha}_l = (\alpha_{l,1}, ..., \alpha_{l,N_\mathrm{D}})^T \in \mathbb{R}^{N_\mathrm{D}}$ is a sparse vector with K non-zero coefficients. Thus, $\boldsymbol{I}_l^K \in \mathbb{R}^{N+1}$ is a sparse approximation of the ISRF $\boldsymbol{I}_l$. The representation (4) and the forward model (1) lead to:

$$\boldsymbol{s}_l \approx \boldsymbol{R}_l \boldsymbol{I}_l^K = \boldsymbol{\Psi}_l \, \boldsymbol{\alpha}_l, \tag{5}$$

with a new dictionary $\boldsymbol{\Psi}_l \triangleq \boldsymbol{R}_l\boldsymbol{\Phi} \in \mathbb{R}^{(L+1)\times N_\mathrm{D}}$. The dictionary $\boldsymbol{\Phi}$ and the reference spectra $\boldsymbol{R}_l$ being known, $\boldsymbol{\Psi}_l$ is also known. Thus, estimating the ISRFs from the measured spectra reduces to finding a sparse vector $\boldsymbol{\alpha}_l$ yielding a good approximation of $\boldsymbol{s}_l$ in (5). The problem can be formulated as in [6] using the l_0 pseudo-norm $||\cdot||_0$ with penalty μ:

$$\arg\min_{\boldsymbol{\alpha}_l} L(\boldsymbol{\alpha}_l, \mu) = \arg\min_{\boldsymbol{\alpha}_l} ||\boldsymbol{s}_l - \boldsymbol{\Psi}_l\boldsymbol{\alpha}_l||_2^2 + \mu||\boldsymbol{\alpha}_l||_0. \tag{6}$$

This problem is non convex and NP-hard, and therefore many approximations and heuristics have been proposed to solve this problem. An approach that previously yielded promising results in this context is the use of the greedy algorithm Orthogonal Matching Pursuit (OMP) [6]–[8].

B. Spectral shift estimation

The characterization of the central wavelengths λ_l and ISRFs $\boldsymbol{I}_l$ is typically performed during ground calibration. However, spectral errors and ISRF modifications may arise in-flight due to uncorrected Doppler shifts or other effects, which can induce spectral shifts in the measured spectra. It makes sense to model these shifts using a polynomial of degree P:

$$\delta(l, \boldsymbol{c}) = \sum_{p=0}^{P} c_p \left(\frac{l}{l_{\max}}\right)^p, \tag{7}$$

where $\boldsymbol{c} = [c_0, ..., c_P]^T \in \mathbb{R}^{P+1}$ is a vector to be estimated and $l_{\max}$ is the number of pixels in the band. Note that a first-order polynomial is used for the spectrometer GOSAT [4], whereas up to fifth-order polynomials are considered for other spectrometers such as OCO-2 [5]. The associated shifted wavelength λ_l' is thus defined by $\lambda_l' = \lambda_l + \delta(l, \boldsymbol{c})$. In this configuration, the vector $\boldsymbol{I}_l$ characterizing the ISRFs is not affected by spectral shifts, contrary to the matrix $\boldsymbol{R}_l$ that should be modified to account for these spectral shifts.

The problem considered to estimate the ISRFs in presence of spectral shifts is defined as:

$$\arg\min_{\boldsymbol{A}, \boldsymbol{c}} g(\boldsymbol{A}, \boldsymbol{c}), \tag{8}$$

where g is defined from (6) with a polynomial model for the spectral shifts as:

$$\begin{aligned}
g(\boldsymbol{A}, \boldsymbol{c}) &\triangleq \sum_{l=1}^{N_\lambda} ||\boldsymbol{s}_l - \boldsymbol{R}_l(\boldsymbol{c})\boldsymbol{\Phi}\boldsymbol{\alpha}_l||_2^2 + \mu \sum_{l=1}^{N_\lambda} ||\boldsymbol{\alpha}_l||_0, \\
\boldsymbol{R}_l(\boldsymbol{c}) &\triangleq \pi\left(\boldsymbol{r}, \mathcal{W}\left(\lambda_l + \sum_{p=0}^{P} c_p \left(\frac{l}{l_{\max}}\right)^p\right)\right),
\end{aligned} \tag{9}$$

where $\boldsymbol{A} = [\boldsymbol{\alpha}_1, ..., \boldsymbol{\alpha}_{N_\lambda}] \in \mathbb{R}^{N_\mathrm{D}\times N_\lambda}$. Estimating the ISRFs and their center wavelengths thus reduces to estimating the sparse vectors $\boldsymbol{\alpha}_1, ..., \boldsymbol{\alpha}_{N_\lambda}$ along with the vector $\boldsymbol{c}$ of the polynomial coefficients modeling the spectral shifts. The estimation method proposed to solve (8) is introduced in the next section.

C. Optimization method

The proposed optimization method solving (8-9) iteratively estimates the ISRFs for a given band and the polynomial coefficients associated with the spectral shifts, as summarized in Algorithm 1. The estimation of $\boldsymbol{A}$ given $\boldsymbol{c}$ is conducted using the OMP algorithm taking into account the sparsity of the vector $\boldsymbol{\alpha}_l$ (see lines 9 and 21 of Algorithm 1). The estimation of the polynomial coefficients (vector $\boldsymbol{c}$) given $\boldsymbol{A}$ is conducted using the Nelder-Mead simplex method [9] with the initialization $\boldsymbol{c} = 0$ (see line 12 of Algorithm 1). This initialization corresponds to an absence of spectral shifts. Note that the first estimation of the ISRF sparse vectors $\boldsymbol{\alpha}_l$ is performed using the first atom of the dictionary (line 9 of Algorithm 1), as it represents an approximate average of all the ISRFs used to build the dictionary. After this first step, the vectors $\boldsymbol{\alpha}_l$ are estimated for fixed $\mathbf{c}$ for the entire band, using the OMP algorithm with K atoms as in [6]. This alternating process continues until convergence.

Algorithm 1 Iterative estimation of ISRFs and spectral shifts.

Input: Measured spectrum $\boldsymbol{s}$, Reference spectrum $\boldsymbol{r}$, Wavelengths $\boldsymbol{\lambda}$, Dictionary $\boldsymbol{\Phi}$, Desired cardinality K , Polynomial order P
Output: ISRF estimation $\hat{\boldsymbol{I}}$, Corrected spectral measurements $\hat{\boldsymbol{s}}$, Spectral shifts $\hat{\boldsymbol{\lambda}}'$.

1: Initialize $\hat{\boldsymbol{c}} = [0, ..., 0]^T$;
2: Initialize $\hat{\boldsymbol{R}}$ with;
3: **for** $l = 1, ..., N_\lambda$: **do**
4: Update: $\hat{\boldsymbol{R}}_l = \pi(\boldsymbol{r}, \mathcal{W}(\lambda_l))$;
5: **end for**
6: Initialize $\hat{\boldsymbol{A}}$ with;
7: **for** $l = 1, ..., N_\lambda$: **do**
8: $\hat{\boldsymbol{\Psi}}_l = \hat{\boldsymbol{R}}_l\, \boldsymbol{\Phi}$;
9: $\hat{\boldsymbol{\alpha}}_l = \text{OMP}(\boldsymbol{s}_l, \hat{\boldsymbol{\Psi}}_l, 1)$;
10: **end for**
11: **while** not convergence **do**
▷ Estimation of the spectral shifts:
12: Update: $\hat{\boldsymbol{c}} = \arg\min_{\boldsymbol{c}} \sum_{l=1}^{N_\lambda} ||\boldsymbol{s}_l - \boldsymbol{R}_l(\boldsymbol{c})\boldsymbol{\Phi}\hat{\boldsymbol{\alpha}}_l||_2^2$;
13: **for** $l = 1, ..., N_\lambda$: **do**
14: Update: $\hat{\lambda}'_l = \lambda_l + \sum_{p=0}^{P} \hat{c}_p \left(\frac{l}{l_{\max}}\right)^p$;
15: **end for**
▷ Interpolation of the reference spectrum:
16: **for** $l = 1, ..., N_\lambda$: **do**
17: Update: $\hat{\boldsymbol{R}}_l = \pi(\boldsymbol{r}, \mathcal{W}(\hat{\lambda}'_l))$;
18: **end for**
▷ Estimation of sparse vectors:
19: **for** $l = 1, ..., N_\lambda$: **do**
20: $\hat{\boldsymbol{\Psi}}_l = \hat{\boldsymbol{R}}_l\, \boldsymbol{\Phi}$;
21: $\hat{\boldsymbol{\alpha}}_l = \text{OMP}(\boldsymbol{s}_l, \hat{\boldsymbol{\Psi}}_l, K)$;
22: **end for**
23: **end while**
▷ ISRF estimation:
24: $\hat{\boldsymbol{I}} = [\boldsymbol{\Phi}\hat{\boldsymbol{\alpha}}_1, ..., \boldsymbol{\Phi}\hat{\boldsymbol{\alpha}}_{N_\lambda}]$
▷ Reconstruction of the spectrum:
25: $\hat{\boldsymbol{s}} = [\hat{\boldsymbol{R}}_1\hat{\boldsymbol{I}}_1, ..., \hat{\boldsymbol{R}}_{N_\lambda}\hat{\boldsymbol{I}}_{N_\lambda}]$
▷ Spectral shift estimation:
26: $\hat{\boldsymbol{\lambda}}' = [\hat{\lambda}'_1, .., \hat{\lambda}'_{N_\lambda}]$

III. Optimal transport

Given the estimated ISRFs $\hat{\boldsymbol{I}}$, the use of the ℓ_2 metric may not always be suitable for estimating spectral shifts. It is particularly true when the spectral shifts are large, which can lead to a cost function with many local minima. This paper proposes to investigate a new distance based on OT theory to better estimates the shift parameter $\boldsymbol{c}$.

A. Optimal transport and Wasserstein distance in 1D

Let $\eta, \xi : \mathbb{R} \to \mathbb{R}_+$ be two non-negative densities, i.e., functions absolutely continuous with respect to the Lebesgue measure on $\mathbb{R}$, and normalized such that

$$\int_{\mathbb{R}} \eta(\lambda)d\lambda = \int_{\mathbb{R}} \xi(\lambda)d\lambda = m,$$

for some $m > 0$. Then, their Wasserstein-2 distance (see, e.g., [10]) is defined as

$$W_2(\eta, \xi) = \left(\inf_{\substack{T:\mathbb{R}\to\mathbb{R} \\ T_\#\eta = \xi}} \int_{\mathbb{R}} (\lambda - T(\lambda))^2 d\lambda \right)^{1/2},$$

where $T_\#\eta$ denotes the push-forward or image measure of η under the map T. The optimal so-called Monge map T can be interpreted as the map rearranging the mass distribution described by the density η to that of ξ so that the overall displacement, or transport, is minimized. Here, displacement is measured by the squared Euclidean distance on $\mathbb{R}$. In fact, as η and ξ are densities, such a (unique) Monge map always exists and is given as [11, Thm. 2.9]

$$T = F_\xi^{[-1]} \circ F_\eta,$$

where F_η and F_ξ are the cumulative distribution functions of η and ξ, and $F_\xi^{[-1]}$ denotes the pseudo-inverse[1] of F_ξ. The Wasserstein-2 distance can then be written in closed form as:

$$W_2(\eta, \xi) = \left(\int_0^m \left(F_\eta^{[-1]}(y) - F_\xi^{[-1]}(y) \right)^2 dy \right)^{1/2}. \quad (10)$$

In our case, the densities η and ξ correspond to the measured and reconstructed spectral densities $\mathbf{s}$ and $\hat{\mathbf{s}}$. Thus, to compute their Wasserstein distance, we approximate (10) by replacing the integrals defining $F_\eta^{[-1]}$ and $F_\xi^{[-1]}$ by Riemann sums.

B. A new metric for spectral shift estimation

OT theory has been used in multiple applications, including high resolution seismic imaging [12]. Due to the convexity of OT distances with respect to translations and dilatations, the Wasserstein distance is an attractive alternative to the ℓ_2 norm. In the case of spectral shift estimation, the measured spectrum $\boldsymbol{s}$ and the reconstructed spectrum obtained using the model should have the same mass to properly define the 1D Wasserstein distance (10). The densities η and $\xi(\boldsymbol{c})$ introduced in Section III are then defined for this problem as the normalized measured spectra and the model depending on the shift parameter $\boldsymbol{c}$, with a mass $m = 1$.

Fig. 2 displays the distances $||\eta - \xi(\boldsymbol{c})||_2$ and $W_2(\eta, \xi(\boldsymbol{c}))$ versus the spectral shifts $\boldsymbol{c}$, assuming that the ISRFs are known. In this example, the true spectral shift is generated identically for all pixels of the band to 0.065 nm, i.e., $P = 0$ and $c_0 = 0.065$. The figure illustrates that the use of the ℓ_2

[1]This formally allows for cases when ξ is zero on intervals.

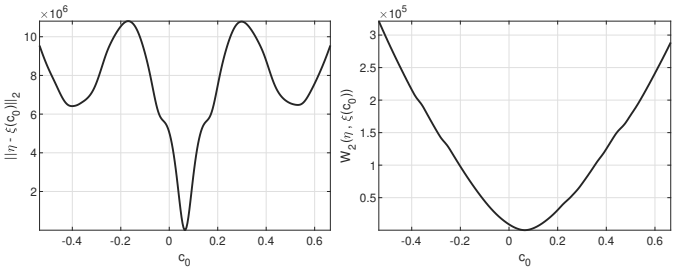

Fig. 2. Distances between the measurements $\boldsymbol{s}_l$ and the statistical model $\boldsymbol{R}_l(\boldsymbol{c})\boldsymbol{\Phi}\boldsymbol{\alpha}_l$ versus the shift value using the ℓ_2 norm (left) and OT (right).

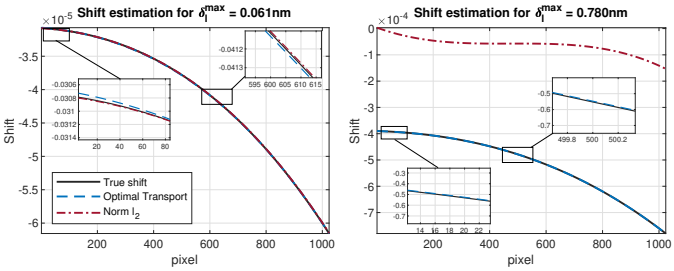

Fig. 3. Spectral shift estimation for SNC1 (left) and SCN2 (right).

norm can lead to a cost function with several local minima, contrary to the Wasserstein distance that defines a well behaved cost functional without local minima, suggesting that the OT metric is more adapted to this situation. The estimation of the spectral shifts performed in line 12 of Algorithm 1 can then be done using the Wasserstein distance. This line is thus modified as: Update $\hat{\boldsymbol{c}} = \arg\min_{\boldsymbol{c}} \sum_{l=1}^{N_\lambda} W_2(\boldsymbol{s}_l, \boldsymbol{R}_l(\boldsymbol{c})\boldsymbol{\Phi}\hat{\boldsymbol{\alpha}}_l)$.

IV. Numerical experiments

A. Datasets and simulation

Data. The data used in this paper results from simulations carried out by the CNES for the MicroCarb mission. The main objective of this mission is to monitor carbon dioxide fluxes at the Earth's surface and determine as accurately as possible the concentration of carbon dioxide in the atmosphere. The MicroCarb instrument is a spectrometer with high spectral resolution acquiring data in two infrared absorption bands (B2: 1.596-1.618μm and B3: 2.023-2.051μm) to recover CO_2 absorption lines, and in two near-infrared bands (B1:0.758-0.769μm and B4: 1.264-1.282μm) to determine oxygen concentration. The results shown in this paper are obtained for the first band B1. The reference spectrum was obtained using a radiative transfer software named 4A/OP [13]. The ISRFs were then obtained using a simulator of the MicroCarb instrument developed by CNES. The spectral shifts were simulated using a polynomial of order $P = 3$.

Experimental setup. The dictionary $\boldsymbol{\Phi}$ is built using the N_{D} singular vectors associated with the largest singular values from a singular value decomposition (SVD) of examples of ISRFs, simulated for the chosen band. The size of the dictionary is N_{D}= 25, and the size of the observation window is L= 80. The number of selected atoms K is set to 4, as in [6]. The performance is evaluated in terms of spectrum reconstruction errors, ISRF approximation and spectral shift estimation using the same metric. More precisely, the error between a true parameter vector $\boldsymbol{\theta} = (\theta[1], ..., \theta[Q])^T$ and its estimation $\hat{\boldsymbol{\theta}}$ is expressed as:

$$\mathrm{E}_{\boldsymbol{\theta}} = \sum_{q=1}^{Q} |\boldsymbol{\theta}[q] - \hat{\boldsymbol{\theta}}[q]| \; / \sum_{q=1}^{Q} |\boldsymbol{\theta}[q]|. \tag{11}$$

B. Results

Spectral shift estimation. Two different scenarios for generating the spectral shifts are assessed. In scenario SCN1, a spectral shift of up to three pixels is generated, resulting in a maximum shift value of 0.061nm. In SCN2, a larger shift of up to thirty pixels is used, associated with a maximum value of 0.78nm. Spectral shift estimates obtained using the proposed algorithm are displayed in Fig. 3. They show that for a shift of three pixels, both metrics provide good results, with slightly superior performance for the ℓ_2 norm. However, when the shift becomes larger (right figure), the use of the ℓ_2 norm becomes challenging for accurately retrieving the spectral shift. In contrast, the OT metric provides reliable results in both scenarios, at the price of increased computational cost.

Joint estimation of ISRFs and spectral shifts. Figures 4 a) and b) display the results obtained in terms of spectrum reconstruction whereas Fig. 4 c) shows the ISRF approximation error for all 1024 wavelengths of the band B1. For spectral shifts up to three pixels (SCN1), the two metrics provide good estimation results both in terms of ISRF approximation errors and spectrum reconstruction, with errors less than 1%. However, when the spectral shifts are larger (SCN2), the ℓ_2-norm based approach fails to estimate the ISRFs, yielding poor ISRF estimates. Using the Wasserstein distance yields significantly better results, with errors comparable to those observed in the SCN1 scenario, at the price of an increased computational time. These results are confirmed in Fig. 5 for the ISRF located at the center of the band.

Robustness to noise. Table I shows results for the above two scenarios for different noise levels. The spectrum reconstruction, mean ISRF approximation and spectral shift estimation errors (defined using (11)) are smaller for larger SNR values, as expected. The OT metric always provides better results than the ℓ_2 norm for larger spectral shifts. As the SNR value increases, the results are very similar, with an OT metric providing slightly better results than the ℓ_2 norm.

V. Conclusion

This paper proposed a new method to jointly estimate instrument spectral response functions (ISRFs) and spectral shifts for spectrometer calibration. The spectral shifts are modeled using a polynomial, but our approach could also handle other parametric model functions. An effective iterative algorithm was proposed, alternating between sparse approximation of ISRFs using OMP and estimation of spectral shift model parameters. As a key original ingredient, a new metric based on optimal transport is studied for the spectral shifts. The Wasserstein-2 distance is used as a heuristic trick that is

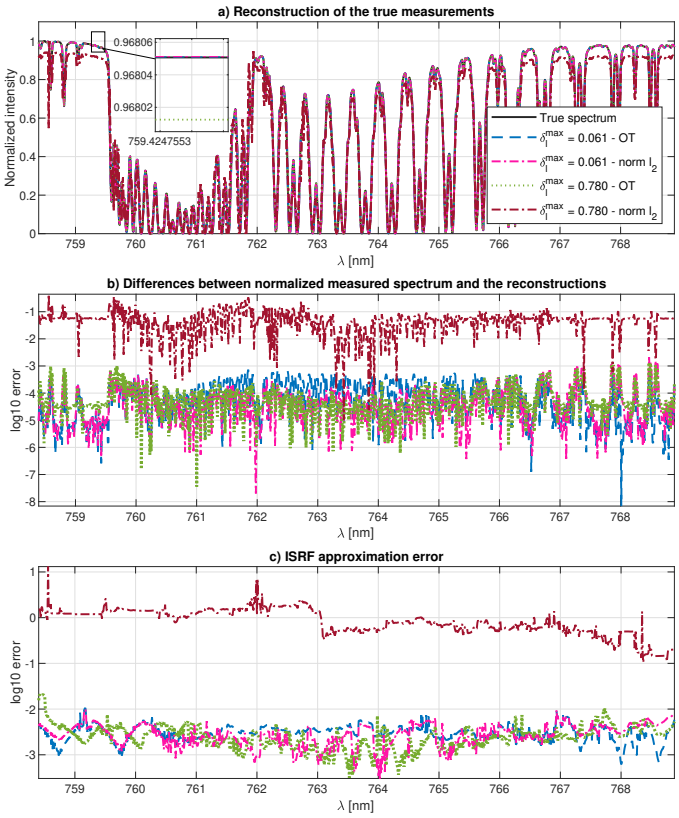

Fig. 4. Estimation performance for the ℓ_2 and OT metrics and the two scenarios (SCN1 and SCN2): a) True spectrum and its reconstruction, b) difference between the true spectrum and its reconstruction c) ISRF approximation error versus wavelength (E_{ISRF}).

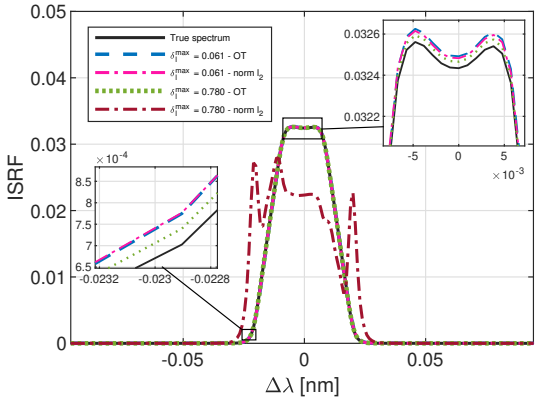

Fig. 5. Examples of estimated ISRFs for the two scenarios SCN1 and SCN2 and the two metrics ℓ_2 and OT.

interesting for its convexity properties and is proposed here as an alternative to the commonly used ℓ_2 norm. An associated theoretical study is left for future work. Simulation results suggest that the proposed joint estimation method yields accurate ISRF and the spectral shift estimates. For spectral shifts are small, both the ℓ_2-norm and Wasserstein-2 based solutions are effective, but for large values of the spectral shifts, the former fails while the Wasserstein-2 norm based approach yields very satisfactory results, at the price of increased computation cost.

TABLE I

SPECTRUM RECONSTRUCTION ERROR (E_{SPECTRUM}), ISRF APPROXIMATION ERRORS (E_{ISRF}) AND SPECTRAL SHIFTS (E_{SHIFTS}) ESTIMATION ERRORS FOR SCN1 AND SCN2 FOR DIFFERENT SNRS AND DIFFERENT METRICS (NORM 2 (l_2) AND OT).

$\times 10^{-2}$	E_{spectrum}		E_{ISRF}		E_{shifts}	
SNR	SCN 1	SCN 2	SCN 1	SCN 2	SCN 1	SCN 2
40 dB l_2	0.026	6.281	0.534	96.45	**1.326**	142.3
OT	**0.019**	**0.021**	**0.499**	**0.700**	7.915	**0.251**
55 dB l_2	**0.017**	6.302	**0.309**	96.58	**0.790**	308.5
OT	0.023	**0.017**	0.320	**0.285**	3.091	**0.144**
80 dB l_2	**0.016**	6.301	0.306	96.51	**0.669**	308.5
OT	0.022	**0.018**	**0.304**	**0.272**	3.147	**0.162**

Future work will study other physical degradations, such as stray light or radiometric errors, and will analyze the potential interest of using other sparse regularizations [14] [15].

REFERENCES

[1] E. Cansot, L. Pistre, M. Castelnau, P. Landiech, L. Georges, Y. Gaeremynck, and P. Bernard, "MicroCarb instrument, overview and first results," *Proc. SPIE 12777, Inf. Conf. Space Optics*, vol. 12777, no. 1277734, pp. 1–13, 2022.

[2] K. Sun, X. Liu, G. Huang, G. González Abad, Z. Cai, K. Chance, and K. Yang, "Deriving the slit functions from OMI solar observations and its implications for ozone-profile retrieval," *Atmos. Meas. Tech.*, vol. 10, no. 10, pp. 3677–3695, 2017.

[3] M. Hamidouche and G. Lichtenberg, "In-flight retrieval of SCIAMACHY instrument spectral response function," *Remote Sens.*, vol. 10, no. 3, pp. 401, 2018.

[4] H. Ye, X. Wang, J. Wu, and Y. Jiang, "A priori estimation for spectral shift of atmospheric carbon dioxide satellite measurement," *Optik*, vol. 158, pp. 283–290, 2018.

[5] K. Sun, X. Liu, C. R. Nowlan, Z. Cai, K. Chance, C. Frankenberg, R. A. M. Lee, R. Pollock, R. Rosenberg, and D. Crisp, "Characterization of the oco-2 instrument line shape functions using on-orbit solar measurements," *Atmos. Meas. Tech.*, vol. 10, no. 3, pp. 939–953, 2017.

[6] J. El Haouari, J.-M. Gaucel, C. Pittet, J.-Y. Tourneret, and H. Wendt, "In-flight estimation of instrument spectral response functions using sparse representations," *Atmos. Meas. Tech.*, p. to be published, 2025.

[7] S. G. Mallat and Z. Zhang, "Matching pursuits with time-frequency dictionaries," *IEEE Trans. Signal Process.*, vol. 41, no. 12, pp. 3397–3415, 1993.

[8] Y. C. Pati, R. Rezaiifar, and P. S. Krishnaprasad, "Orthogonal matching pursuit: recursive function approximation with applications to wavelet decomposition," in *Proc. Asilomar Conf. Signals, Systems and Computers*, Pacific Grove, CA, USA, Nov. 1-3 1993, pp. 40–44.

[9] J. C. Lagarias, J. A. Reeds, M. H. Wright, and P. E. Wright, "Convergence properties of the Nelder-Mead simplex method in low dimensions," *SIAM J. Optim.*, vol. 9, pp. 112–147, 1998.

[10] C. Villani et al., *Optimal transport: old and new*, vol. 338, Springer, 2009.

[11] F. Santambrogio, "Optimal transport for applied mathematicians," *Birkäuser, NY*, vol. 55, no. 58-63, pp. 94, 2015.

[12] L. Métivier, R. Brossier, F. Kpadonou, J. Messud, and A. Pladys, "A review of the use of optimal transport distances for high resolution seismic imaging based on the full waveform," *MathematicS In Action*, vol. 11, no. 1, pp. 3–42, 2022.

[13] NOVELTIS, CNES, and LMD, "4A/OP - operational release for 4A - automatized atmospheric absorption atlas," https://4aop.noveltis.fr/references-and-publications.

[14] Jihanne El Haouari, Marcus Carlsson, Jean-Yves Tourneret, Herwig Wendt, Jean-Michel Gaucel, and Christelle Pittet, "Estimating instrument spectral response functions using sparse representations and quadratic envelopes," in *Proc. IEEE Int. Conf. Acoust., Speech Signal Process. (ICASSP)*, 2025, pp. 1–5.

[15] Z.-Y. Wang, H. C. So, and A. M. Zoubir, "Low-rank tensor completion via novel sparsity-inducing regularizers," *IEEE Trans. Signal Process.*, vol. 72, pp. 3519–3534, 2024.